Eigendegradation algorithm applied to visco-plastic weak layers

Pedro Navas [1] ![ORCID] **, Diego Manzanal**[1] ![ORCID] *****, **Susana López-Querol** [2] ![ORCID] **Angel Yagüe**[1] ![ORCID] **and Miguel Martín Stickle** [1] ![ORCID]

[1]   Universidad Politécnica de Madrid. ETSI Caminos, Canales y Puertos. Prof. Aranguren 3, Madrid.
[2]   Department of Civil, Environmental and Geomatic Engineering, University College London, Gower Street, London WC1E 6BT, UK
*   Correspondence: d.manzanal@upm.es

Abstract: The time dependence of soil behavior is of particular interest for embankments in soft clays, shear band progression in slopes or where the speed of the load application affects the bearing capacity of the material. This study extends non-local failure, algorithms such as Eigenerosion and Eigensoftening, in order to evaluate the failure of weak layers. In particular, the time dependence of shear band progression is analyzed through the integration of a Perzyna-type visco-plastic model with a degradation algorithm within the Optimal Transportation Meshfree (OTM) framework. The validation of the proposed algorithm is carried out through three practical cases.

1. Introduction

The failure of geomaterials has been a topic of study since the early work of Coulomb in 1877. It has been developed theoretically in soil mechanics since the work of Drucker and Prager [1]. Failures are idealized into two types depending on the state of the material: diffuse and localized.

Diffuse failures are associated with the instability of loose and saturated materials (e.g. [2], [3]) under monotonic and dynamic loads. The increase of the pore pressure leads the material to liquefy, reduces the material's effective stresses to zero, and provokes landslides involving large volumes of material. Numerical modeling of diffuse failure initiation has been developed in finite elements to reproduce failures in mine tailing dams ([4], [5]), to reproduce landslide failures ([6], [7]) or the study of loose saturated material under seismic action ([8], [9]). Recently, these phenomena have been studied with meshfree techniques, allowing to evaluate the transition from solid to fluidized materials with SPH techniques with one (e.g. [3], [10], [11], [12], [13]) and two phases ([14], [15]), Material Point Method, MPM, (e.g. [16–18]) and Discrete Element Methods, DEM, for the liquefaction on granular materials (e.g. [19], [20]).

In contrast, localized failures are associated with strain concentration in a narrow zone and a limited region, which produces a discontinuity in the deformation as well as in the strain rate. This failure is related to a weak discontinuity, also known as a weak layer. The progress of the failure of overconsolidated clays that present a softening behavior has been studied extensively. It consists of a reduction of the shear strength from the peak to the residual value. Early work by Rice [21] provided the theoretical basis for understanding the physics and mathematics of the problem. The formation and propagation of shear bands have been studied through theoretical and lab-scale models (e.g. [22], [23]). Numerically, the localization of shear deformations associated with softening behaviors, which is related to negative slopes in the loading-displacement curve, traditionally depends on the mesh discretization (e.g.[24]. The employment of visco-plastic models has allowed the regularization of the problem (e.g. [25]).

39   Visco-plastic formulations have been developed to evaluate the rate-dependent
40 failure of geomaterials, shear bands, creep and stress relaxation. In general, such constitu-
41 tive formulations include empirical models focused on the evaluation of creep and stress
42 relaxation for soft clays ([26], [27]), rheological models for a wide range of deformations
43 (e.g. [28], [11], [29]) and general stress-strain-time constitutive models (e.g.[30], [31]).
44 Elasto-plastic constitutive models incorporating rate dependence are based mainly on
45 the over-stress theory ([32]) and on the concept of a non-stationary flow surface (e.g.
46 [33], [34]). The over-stress theory assumes no viscous strains occur inside the static yield
47 surface (elastic region). However, the inelastic region is rate dependent. This depen-
48 dency is defined by an over-stress factor. This theory has been implemented in finite
49 element and meshfree methods to study different geotechnical problems (e.g.[29,35]).

50   In this paper, we propose a methodology for evaluating the progression of a shear
51 band or a weak layer through a phenomenological viscoplastic model, taking the benefits
52 of a non-local failure approach. The proposed algorithm is based on the same principles
53 of both Eigenerosion and Eigensoftening approaches, which have been widely employed
54 through material point-based frameworks in order to assess the fracture evolution in
55 quasi brittle materials ([36], [37]) once specific energy (Eigenerosion) or stress (Eigensoft-
56 ening) thresholds are reached when the material point fails. Within the aforementioned
57 algorithms, the failure can be modeled instantaneously (Eigenerosion) or following a
58 material-dependent softening law (Eigensoftening). In order to achieve a diffuse failure
59 through the degradation of the material, a combination of these algorithms within a
60 Perzyna-type viscoplastic model is proposed. This methodology is validated together
61 with a particle-based discretization (OTM) with three practical cases: a) the progression
62 of a shear band, b) the effect of the velocity on the ultimate load of a footing and c) the
63 failure of a vertical slope with a weak layer.

64   Therefore, with the aim of verifying the good performance of the aforementioned
65 algorithm, the rest of the paper is organized as follows. In section 2, the constitutive
66 model with all its ingredients (rate dependent plasticity and non-local failure procedure)
67 is presented; in section 3, time and spatial discretizations are outlined; in section 4,
68 several applications are depicted; and, finally, conclusions are provided in section 5.

69 **2. Constitutive model**

70 *2.1. Rate dependent plasticity*

71   Along with the mathematical and numerical models described so far, it is essential
72 to choose an appropriate constitutive model for the materials. It has been studied how
73 soft clays suffer a viscous phenomenon and delayed deformation due to creep behavior
74 ([26]). The concept of the viscoplastic model described in this section and used in the
75 further simulations is based on Perzyna's theory [32]. Perzyna's theory is a modification
76 of classical plasticity, wherein viscous-like behavior is introduced by a time-rate flow
77 rule employing a dynamic plasticity yield function. Similar to the rate-independent
78 theory, the strain rate is decomposed into an elastic and a viscoplastic strain rate:

$$\dot{\boldsymbol{\varepsilon}} = \dot{\boldsymbol{\varepsilon}}^{\mathrm{e}} + \dot{\boldsymbol{\varepsilon}}^{\mathrm{vp}} \tag{1}$$

79   The stress rate tensor $\dot{\sigma}$ is related to the elastic strain rate via a constitutive tensor
80 $\boldsymbol{D}_e$, which is constant in the case of linear elasticity and variable (stress dependent) in
81 the case of hypo or hyperelasticity:

$$\dot{\sigma} = \mathbf{D}_e(\dot{\varepsilon} - \dot{\varepsilon}^{vp}) \tag{2}$$

82   In the theory proposed by Perzyna [32], and later modified by Souza-Neto *et al.* [38],
83 the viscoplastic strain rate is defined in a similar fashion as in the rate independent
84 plasticity theory:

$$\dot{\boldsymbol{\varepsilon}}^{\mathrm{vp}} = \langle \dot{\lambda} \rangle \frac{\partial g}{\partial \boldsymbol{\sigma}} \tag{3}$$

where $\langle \dot{\lambda} \rangle$ is the viscous flow function, which represents the current magnitude of viscoplastic strain rate. g denotes the viscoplastic potential function and f any valid plasticity function playing the role of loading surface. A von Mises yield surface, with a degradation curve for the undrained shear strength, has been adopted for the failure criteria. Associative flow is invoked by $f = g.\frac{\partial g}{\partial \sigma}$ that represents the current direction of the viscoplastic strain rate. The viscous flow function is defined by:

$$\langle \dot{\lambda} \rangle = \left\{ \begin{array}{ll} \gamma \left[\left(\frac{q}{\sigma_y} \right)^\alpha - 1 \right] & , \phi > 0 \\ 0 & , \phi \leq 0 \end{array} \right. , \tag{4}$$

where $<>$ denotes Macauley brackets, γ is the fluidity parameter (which is the reciprocal of viscosity) and α is a material constant. Function ϕ is defined as:

$$\phi = q - \sigma_y, \tag{5}$$

where q is the deviatoric stress invariant and σ_y is defined by the degradation law which will be detailed later. Concerning algorithm aspects, in displacement-based finite element formulations, stress updates take place at the Gauss points for a known nodal displacement. We start from time t_n with the known converged state:

$$\left[\varepsilon_n, \varepsilon_n^{vp}, \sigma_n, \kappa_n \right] \tag{6}$$

(namely total strain, viscoplastic strain, stress and a scalar internal variable that characterizes the size of the loading surface for the purpose of introducing hardening or softening behavior) to calculate the corresponding values at time

$$t_{n+1} = t_n + \Delta t : \left[\varepsilon_{n+1}, \varepsilon_{n+1}^{vp}, \sigma_{n+1}, \kappa_{n+1} \right]. \tag{7}$$

Indeed, this process has been carried out in an incremental way, being calculated:

$$\Delta \varepsilon = \varepsilon^e + \Delta \varepsilon^{vp} \tag{8}$$
$$\Delta \sigma = \mathbf{D}_e (\Delta \varepsilon - \Delta \varepsilon^{vp}) \tag{9}$$

Therefore, the key feature of the stress updates is characterized by estimating the incremental viscoplastic strain $\Delta \varepsilon^{vp}$. Details of the numerical implementation can be found in the textbooks (Owen and Hinton, 1986 [39]; De Souza Neto *etal.*, 2008 [38]). It has to be noticed also that for softening problems the viscoplasticity approach has a regularizing effect in the sense that the initial-value problem remains well-posed avoiding instability due to strain and strain-rate softening (Wang *etal.* [24].

2.2. Eigenerosion and Eigensoftening algorithms

Within the context of OTM formulation, fracture can be modeled simply by eroding material points according to an energy-release criterion or stress criterion depending on whether the eigenerosion [40–43] or the eigensoftening [36,37,44] algorithm is adopted respectively. In both methodologies, when the material points are failed, they are neglected from the computation of stresses in the model, which approximates the presence of cracks. However, the way to reach the zero stiffness state is different for each model: meanwhile in the eigenerosion the failure is instantaneous, in the eigensoftening the material follows a softening curve which depends on the material. It needs to be pointed out that when a material point satisfies the erosion condition, its contribution to the internal force vector and to the material stiffness matrix is set to zero, but its contribution to the mass matrix is maintained. The mass of a material point is discarded only when an eroded material point is not connected to any nodes.
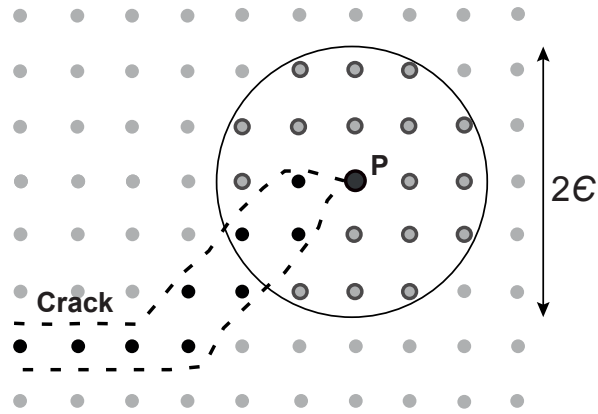
Figure 1. Scheme of a fractured layer (black dots) as set of failed material points, and of the ϵ-neighborhood (inside the circle) of the material point located at the crack tip (gray dots).

Next we compute the energy-release rate attendant to the failure of the material point p, the starting point of the aforementioned methodologies:

$$
\begin{aligned}
G_{p,k+1} &= \frac{C\epsilon}{m_{p,k+1}} \sum_{x_{q,k+1} \in B_\epsilon(x_{p,k+1})} m_q W_k(F_{q,k+1}), \\
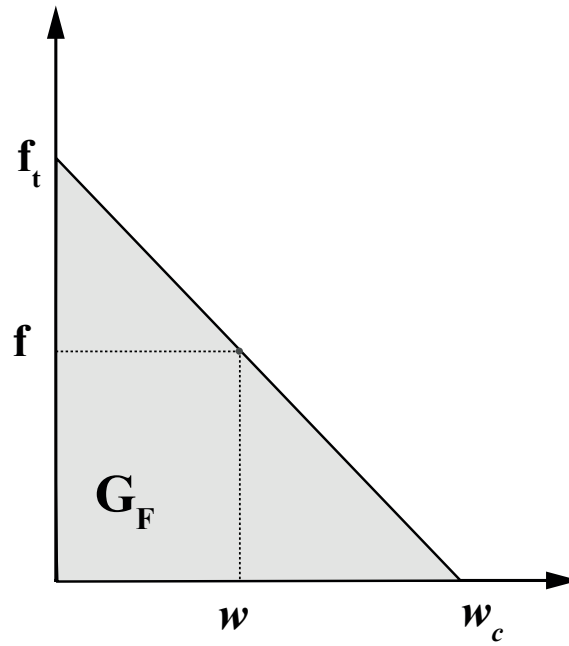m_{p,k+1} &= \sum_{x_{q,k+1} \in B_\epsilon(x_{p,k+1})} m_q,
\end{aligned}
\tag{10}
$$

where $B_\epsilon(x_{p,k+1})$ is the sphere of radius ϵ centered at $x_{p,k+1}$ known as the ϵ-neighborhood of the material point, $m_{p,k+1}$ is the mass of the neighborhood at loading step $k+1$, $W_k(F_{q,k+1})$ is the current free-energy density per unit mass at the material point $x_{q,k+1}$ and C is a normalizing constant, which ranges from 1 to 2, in order to extend the influence from the first line of neighbors to the second [40,41].

The material point is failed when $G_{p,k+1}$ surpasses a critical energy release rate that measures the material-specific energy, G_F, required to create a fracture surface of unit area. In calculations, the failed material-point set is updated at every time step according to this criterion. For linear elasticity, Schmidt *et al*. [40] have shown that this approximation converges to Griffith fracture in the limit of an infinitely fine discretization. Indeed, erosion schemes that estimate the energy-release rate based on the energy of a single material point suffer from mesh-dependency and may overestimate the toughness of the material.

A scheme of the configuration of the ϵ-neighborhood is plotted in Fig. 1.

On the other hand, the implementation of the eigensoftening algorithm consists in adopting a strength criterion for crack initiation and a softening law which is proper to the material under study before the formation of a stress-free crack. This second process tends to accumulate less energy until the crack. When the maximum tensile strength, f_t, is reached, a cohesive crack is formed with zero opening displacement. Once the opening displacement, w, reaches a critical vale, w_c, a stress-free crack is attained. The energy below the softening curve represents the static fracture energy per unit of area, G_F, which is sketched in Fig. 2. For the Eigensoftening calculation, Eq. (10) can be rewritten in terms of the principal stresses at time t_{k+1}, since this model employs the first principal stress as a failure criterion. Therefore, the variation of the averaged strain energy density in the ϵ-neighborhood of the material point $x_{p,k+1}$ can be expressed as,

$$
\delta W_p^\epsilon = \frac{\partial G_p}{C\epsilon} = \frac{1}{m_p} \sum_{x_q \in B_\epsilon(x_p)} m_q \sigma_{q,1} \delta \varepsilon_q,
\tag{11}
$$

Version July 13, 2022 submitted to *Appl. Sci.*

5 of 21

Figure 2. Scheme of a linear cohesive law, where the shade area is G_F, f_t is the tensile strength, and w_c is the critical opening displacement.

where $\sigma_{q,1}$ is the maximum principal stress at a neighboring material point $x_{q,k+1}$. Considering an effective strain ε_q at the material point $x_{q,k+1}$, such that the variation of the local strain energy can be obtained as $\delta W_q = \sigma_{q,1}\delta\varepsilon_q$, let assume the effective strain increment of each material point can be approximated by its counterpart in the neighborhood, being Eq. (11) simplified as:

$$\delta W_p^\epsilon = \frac{\delta\varepsilon_p}{m_p} \sum_{x_{q,k+1}\in B_\epsilon(x_{p,k+1})} m_q\sigma_{q,1}. \tag{12}$$

Thus, the equivalent critical stress at the material point $x_{p,k+1}$ is defined as follows

$$\sigma_p^\epsilon = \frac{1}{m_p} \sum_{x_{q,k+1}\in B_\epsilon(x_{p,k+1})} m_q\sigma_{q,1} \tag{13}$$

136   When $\sigma_{p,k+1}^\epsilon$ surpasses the tensile strength, f_t, the softening behavior is activated
137 through the damage variable χ, which ranges between zero (an intact material) and one
138 (completely failed material points). Of course, χ depends on the current and critical
139 opening measures, w and w_c respectively. The latter is a material parameter, but the first
140 one has to be measured in terms of the achieved strain and a length of affection called
141 band width, h_ϵ, equivalent to the crack band model of Bažant [45]. It bears emphasis
142 that a reference value for h^ϵ is between two and four times the maximum size of the
143 aggregates for concrete according to Bažant [46]. Thus, this is a material parameter more
144 than a numerical artifact. The relationship between strain and crack opening depends
145 on the effective fracture strain, ε_f^ϵ, defined as the difference between the strain at crack
146 initiation, $\varepsilon_1(x_{p,0})$, and the current strain, $\varepsilon_1(x_{p,k+1})$ for a material point p; and the band
147 width as:

$$\varepsilon_f^\epsilon = \varepsilon_1(x_{p,k+1}) - \varepsilon_1(x_{p,0}) = \frac{w}{h^\epsilon} \tag{14}$$

2.3. Eigendegradation model

Following the work of Einav and Randolph [47], and the later implementations of Zhang *et al.* [47] (similar also of some other implementations [48,49]), the behavior of sensitive clays can be modeled by strain softening curves in order to reduce the strength of the material by a degradation obtained by accumulation of strain. Einav and Randolph assumed that the current shear strength depends on the accumulated absolute shear strain, ξ, which is taken as a state variable from which an isotropic strength reduction, $\delta(\xi)$, is calculated as

$$\delta(\xi) = s_u/s_{ui} = \delta_{\text{rem}} + (1 - \delta_{\text{rem}})e^{-3\xi/\xi_{95}} \tag{15}$$

where

$$\xi = \int_t |\dot{\gamma}_{\text{max}}| dt \tag{16}$$

and $|\dot{\gamma}_{\text{max}}|$ is the cumulative absolute shear strain, s_u and s_{ui} are the softened strength and initial strength, respectively, δ_{rem} is the fully remolded strength ratio, and ξ_{95} is the cumulative shear strain required to cause 95% reduction (from peak to remolded). The assumption is that δ_{rem} may be taken as the inverse of the sensitivity of the soil, while an appropriate value for ξ_{95} must be deduced from laboratory test data, or by conducting cyclic penetration and extraction tests with T-bar or ball.

The calculation of the cumulative shear strain can be achieved by the eigendeformation technique, departing from Eq. (11), and considering, for the Eigendegradation calculation, that the stress remains constant in a neighborhood ϵ. Thus, Eq. (11) can be simplified as

$$\delta W_p^\epsilon = \frac{\delta \tau_p}{m_p} \sum_{x_{q,k+1} \in B_\epsilon(x_{p,k+1})} m_q \gamma_q, \tag{17}$$

being $\delta\tau_p$ the increment of tangential stress of the neighborhood and γ_p^ϵ the current local shear strain, calculated as:

$$\gamma_p^\epsilon = \frac{1}{m_p} \sum_{x_{q,k+1} \in B_\epsilon(x_{p,k+1})} m_q \gamma_q \tag{18}$$

Similarly, in the neighborhood ϵ, the non-local cumulative strain of a material point p is calculated, only when plasticity is activated, as follows:

$$\xi_p^\epsilon = \int_{t_{p0}}^{t_{k+1}} \left|\dot{\gamma}_p^\epsilon\right| dt \tag{19}$$

being t_{k+1} referred to the current step and t_{p0} to the step when plasticity begins.

Considering only shear failure, yield shear stress τ is equivalent to the softened strength, s_u, and the residual yield shear stress, τ_{95}, can be reached by $\tau_{95} = \tau rem = s_{ui} \delta_{rem}$. Thus, in every state of degradation, the current yield shear stress, referred to the epsilon neighborhood, τ^ϵ, reads:

$$\tau^\epsilon = \tau_{95} + (\tau_i - \tau_{95})e^{-3\xi_p^\epsilon/\xi_{95}} \tag{20}$$

It is remarkable that, in laboratory, parameter ξ_{95} is not obtained. Instead, the displacement δ_{95} is achieves. In Fig. 3.A) the degradation of the strength in terms of the displacement is plotted. It can be seen how this law can be translated to the shear strain measurement (Fig. 3.B) by multiplying by ϵ, which, in this problem, is considered as the sliding length. Depending on the size of the soft layer, this parameter ϵ is obtained as the minimum length between the neighbor radius and the size of the soft layer (See Fig. 4) as follows:

$$2\epsilon = \min(h_s, 2C_\epsilon h) \tag{21}$$
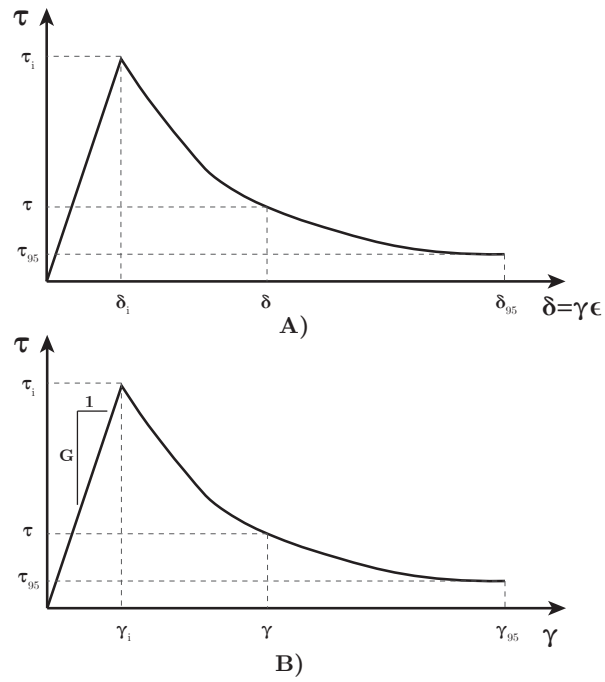
Figure 3. Degradation curve in terms of the displacement, A), and the shear strain, B).
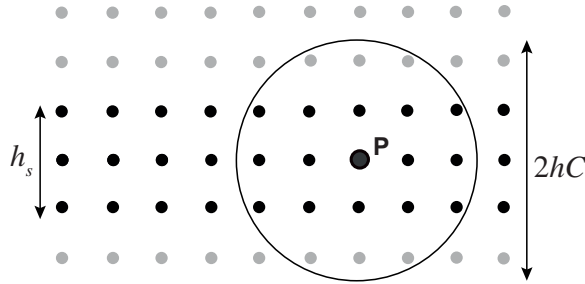
Figure 4. Scheme of the measurements of the soft layer (black dots) and the ϵ-neighborhood around material point P.

2.4. Visco-Plastic Eigendegradation algorithm

Following, the pseudo-algorithm for the Eigendegradation model within a visco-plastic yield surface will be presented. It is worth mentioning that, prior to the algorithm steps, we need to calculate the equivalent shear total strain of every material point as the norm of the deviatoric total strain tensor. Since large strain is considered, the strain tensor is obtained through the logarithm of the left Cauchy-Green strain tensor, **b**:

$$\varepsilon = \frac{1}{2} \log b = \frac{1}{2} \log FF^T. \tag{22}$$

The aforementioned procedure can be followed in Algorithm 1.

3. Time and spatial discretization

Following, the rest of computational tools that were employed in the present research are highlighted. First, the spatial discretization is shown, while the time discretization is mentioned in the final subsection.

Algorithm 1 Visco-Plastic Eigendegradation algorithm

---

1. Calculation of the small strain tensor

$$\varepsilon_{k+1}^{e\ trial} = 1/2 \log \mathbf{b}_{k+1}^{e\ trial}$$

2. Elastic Predictor: volumetric and deviatoric stress measurements

$$\text{Volumetric: } p_{k+1}^{trial} = K \left(\varepsilon_{vol}^e \right)_{k+1}^{trial}$$
$$\text{Deviatoric: } \mathbf{s}_{k+1}^{trial} = 2G \left(\varepsilon_{dev}^e \right)_{k+1}^{trial}$$

$$\text{being: } \sigma_{k+1}^{trial} = J^{-1} \tau_{k+1}^{trial}$$

$$\text{and: } q_{k+1}^{trial} = \sqrt{\tfrac{3}{2}} \| \mathbf{s}_{k+1}^{trial} \|$$

3. Eigendegradation calculation:

if $t < t_{p0}$ **then** $\qquad \sigma_y = \tau_i$
else

- $m_p = \sum_{x_{q,k+1} \in B_\epsilon(x_{p,k+1})} m_q$

- $\gamma_p^\epsilon = \frac{1}{m_p} \sum_{x_{q,k+1} \in B_\epsilon(x_{p,k+1})} m_q \gamma_q$

- $\xi_p^\epsilon = \sum_{k(t_{p0})}^{k+1} \left| \Delta \gamma^\epsilon(x_{p,k}) \right|$

- $\sigma_y = \tau_{95} + (\tau_i - \tau_{95}) e^{-3\xi_p^\epsilon / \xi_{95}}$

- Hardening modulus: $\qquad H = \frac{\partial \sigma_y}{\partial \bar{\varepsilon}^p} \simeq \frac{\partial \sigma_y}{\partial \xi_p^\epsilon} = - \frac{3(\tau_i - \tau_{95})}{\xi_{95}} e^{-3\xi_p^\epsilon / \xi_{95}}$

end if

4. Yield condition: $\Delta \lambda = 0$

if $\phi = q_{k+1}^{trial} - \sigma_y \leq 0$ **then** Elastic region: $\qquad \sigma_{k+1} = \sigma_{k+1}^{trial}$

else Viscoplastic flow:

- **4.1** Derivative of the yield surface:

$$d = \frac{\partial \phi}{\partial \Delta \lambda} = - \left(3G + \alpha \frac{q_{k+1}^{trial} - 3G\Delta\lambda}{\Delta\lambda + \gamma\Delta t} \right) \left[\frac{\gamma\Delta t}{\Delta\lambda + \gamma\Delta t} \right]^\alpha - H$$

- **4.2** Increment of plastic strain: $\Delta \lambda = \Delta \lambda - \frac{\phi}{d}$

- **4.3** Yield function: $\qquad \phi = \left(q_{k+1}^{trial} - 3G\Delta\lambda \right) \left[\frac{\gamma\Delta t}{\Delta\lambda + \gamma\Delta t} \right]^\alpha$

- **4.4** If $\phi < tolerance$ go to **4.5**, else go to **4.1**
- **4.5** Update

$$\bar{\varepsilon}_{k+1}^p = \bar{\varepsilon}_k^p + \Delta\gamma$$

$$\Delta\varepsilon_{k+1}^p = \frac{\Delta\gamma}{\| \mathbf{s}_{k+1}^{trial} \|} \mathbf{s}_{k+1}^{trial}$$

$$\sigma_{k+1} = \left(p_{k+1}^{trial} \right) \mathbf{I} + \left(1 - \frac{3G\Delta\gamma}{q_{k+1}^{trial}} \right) \mathbf{s}_{k+1}^{trial}$$

end if

5. Update elastic left Cauchy-Green Tensor

$$\varepsilon_{k+1}^e = \varepsilon_{k+1}^{e\ trial} - \Delta\varepsilon_{k+1}^p$$

$$\mathbf{b}_{k+1}^e = \exp(2\varepsilon_{k+1}^e)$$

3.1. Spatial discretization

The dynamic problem of a dry soil (mono-phase material) is studied in this research, being the time an important issue of the following analyses. The governing equation of the dynamic problem can be defined by the linear momentum balance equation:

$$\text{div } \sigma - \rho a + \rho g = 0. \tag{23}$$

The derivation of the weak form of the problem needs the multiplication by the test
function δu, the virtual displacement, and the integration over the domain. After the
application of the Green's Theorem, Equation (23) yields:

$$-\int_\Omega \sigma : \text{grad}\delta u \, d\Omega + \int_{\Gamma_t} \delta u \cdot \bar{t} \, d\gamma - \int_\Omega \delta u \cdot \rho a \, d\Omega + \int_\Omega \delta u \cdot \rho g \, d\Omega = 0 \tag{24}$$

where Ω represents the volume of the body and Γ the boundary where tractions are applied. The first term of the equation is defined as the internal forces, meanwhile the second and forth conform the external forces. The next step is the interpolation through the Optimal Transportation Meshfree [50–52], a meshfree method that has been demonstrated to perform reasonably well in geotechnical problems [53,54]. It is based in the conjunction of material points and nodes. As mentioned before, the shape functions are based on the work of Arroyo and Ortiz [55], who defined the Local Max-Ent shape function (LME) of the material point (x) with respect to the neighborhood (x_a) as follows:

$$N_a(\mathbf{x}) = \frac{\exp\left[-\beta_{LME} \, |\mathbf{x} - \mathbf{x_a}|^2 + \lambda^* \cdot (\mathbf{x} - \mathbf{x_a})\right]}{Z(\mathbf{x}, \lambda^*(\mathbf{x}))}, \tag{25}$$

where the computation is done along a neighborhood N_b and

$$Z(\mathbf{x}, \lambda) = \sum_{a=1}^{Nb} \exp\left[-\beta_{LME} \, |\mathbf{x} - \mathbf{x_a}|^2 + \lambda \cdot (\mathbf{x} - \mathbf{x_a})\right]. \tag{26}$$

The first derivatives of the shape function can be obtained from the own shape function
and its Hessian matrix **J** by employing the following expression:

$$\nabla N_a^* \quad = \quad -N_a^* \, (\mathbf{J}^*)^{-1} \, (\mathbf{x} - \mathbf{x_a}), \tag{27}$$

The parameter β_{LME} defines the shape of the neighborhood, and it is related with the discretization size (or nodal spacing), h, and the constant, γ_{LME}, which controls the locality of the shape functions, as follows,

$$\beta = \frac{\gamma_{LME}}{h^2}. \tag{28}$$

It bears emphasis that $\lambda^*(\mathbf{x})$ comes from the minimization of the function $g(\lambda) =$
$\log Z(\mathbf{x}, \lambda)$ to guarantee the maximum entropy.

By employing the outlined shape functions and applying Galerkin procedure to the weak form, u can be interpolated by employing:

$$u \approx u^h = N_u \cdot \tilde{u} \tag{29}$$

where $\square^h$ represents the OTM approximation of the field $\square$ and $\tilde{\square}$ the nodal values. $N_u =$
$[N_1 I, N_2 I, ..., N_m I]$ represents the shape function and m is the number of nodes. Since
the shape functions are defined in the reference configuration and time independent,
$N = N(X)$, the following property holds: $\dot{\square}^h = N \cdot \dot{\tilde{\square}}$.

Table 1: The α-parameters of the Newmark scheme.

$$\alpha_1 = \frac{1}{\beta \Delta t^2} \qquad \alpha_2 = \frac{1}{\beta \Delta t} \qquad \alpha_3 = \frac{1}{2\beta} - 1$$

3.2. Time discretization

In this work, an implicit scheme has been proposed, since several applications cover a wide range of loading rates; from slow scenarios to quick phenomena. For the first ones, an explicit scheme would provide long computation time. Thus, the Newmark Implicit Scheme has been employed, with the parameters $\gamma =0.6$ and $\beta =0.325$ that are known to be suitable for dynamic problems [56]. To construct this scheme, Eq. (24) is reformulated as a system of equations, read as

$$\boldsymbol{R}_{k+1} + \boldsymbol{M}\,\ddot{\boldsymbol{u}}_{k+1} = \boldsymbol{P}_{k+1}, \tag{30}$$

where $\boldsymbol{R}$ and $\boldsymbol{M}$ respectively denote the internal forces vector and mass matrix, whereas $\boldsymbol{P}$ is the external forces vector, which contains both gravity acceleration and external nodal forces. $k+1$ represents the current step. Eq. (30) can be re-written with the Newmark scheme as:

$$\boldsymbol{G}_{k+1} \quad = \quad \boldsymbol{M}\left[\alpha_1 \Delta \boldsymbol{u}_{k+1} - \alpha_2 \dot{\boldsymbol{u}}_k - \alpha_3 \ddot{\boldsymbol{u}}_k\right] + + \boldsymbol{R}_{k+1} - \boldsymbol{P}_{k+1} = \boldsymbol{0}, \tag{31}$$

where the α-parameters are listed in Table 1 according to Wriggers [57]. These coefficients can be easily extended to any other time integration schemes.

Solving the above non-linear equations with a Newton-Raphson method, the resulting iterative scheme, taking into account the matrices that are involved in our problem, can be written as:

$$\left[\alpha_1 \boldsymbol{M} + \boldsymbol{K}_{k+1}^i\right] \Delta \boldsymbol{u}_{k+1}^{i+1} = [\boldsymbol{K}_*]_{k+1}^i \Delta \boldsymbol{u}_{k+1}^{i+1} \quad = \quad -\boldsymbol{G}(\boldsymbol{u}_{k+1}^i), \tag{32}$$
$$\text{where} \quad \boldsymbol{u}_{k+1}^{i+1} \quad = \quad \boldsymbol{u}_{k+1}^i + \Delta \boldsymbol{u}_{k+1}^{i+1}.$$

where $\boldsymbol{K}$ is the tangential stiffness matrix:

$$\boldsymbol{K}(\boldsymbol{u}_{k+1}^i) = \boldsymbol{K}_{k+1}^i = \left.\frac{\partial \boldsymbol{R}}{\partial \boldsymbol{u}}\right|_{\boldsymbol{u}_{k+1}^i}. \tag{33}$$

and i depicts the iteration index. The iteration finishes when $\boldsymbol{G}_{k+1}^i$ is smaller than a given tolerance.

4. Applications

Three tests have been studied in this research. The two first applications are devoted to show the performance of the two main principal properties of the proposed constitutive model: the degradation (Shear test, Sec. 4.1) and the viscous behavior (Strip footing load, Sec. 4.2). The last example shows the suitability of the model when the triggering and propagation of a slope due to cyclic loading is sought.

4.1. Shear test

In the first example, the behavior of a weak layer under a shear test is analyzed. In Fig. 5 an embankment of 10 meters of depth is presented. A weak layer in the bottom of the domain of 0.5 meters appears. The proposed shear test is similar to the one proposed by Zhang *et al.* [47]. Although different constitutive laws are employed (local and non-local), since both are based on similar degradation processes, it is expected to obtain comparable results.

The original embankment's length is 700 m. Since the softened zone only extends 90 m. and considering infinite conditions at both sides of this softened zone, only this 90 m.

Table 2: Parameters for the shear degradation analysis.

Softened/modeled length $L = l_0$	90 m
Overall height, H	10 m
Height of sliding material, h	7.2 m
Shear band thickness, s	0.5 m
Submerged density of the soil, ρ	600 kg/m^3
Poisson's ratio, ν	0.495
Young's modulus, E	1.98 MPa
Peak shear strength, $\tau_p = \tau_i$	10 kPa
Residual (95%) shear strength, $\tau_{95} = \tau_r$	1.25 kPa
Plastic shear strain to 95% reduction in strength, γ_p	0.6
Neighborhood parameter, C_ϵ	1.5
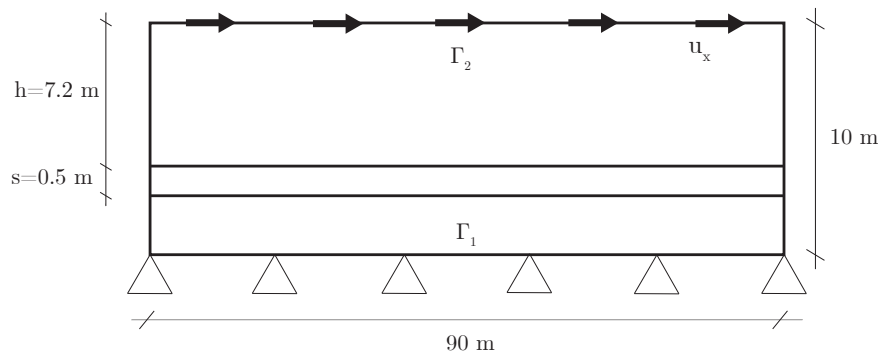
Figure 5. Geometry and loading conditions of the shear degradation problem.

are modeled in order to save computational time. Unlike the original example, gravity conditions are neglected, considering the failure of the embankment at the final of the residual strength. Thus, the parameters needed in this example are shown in Table 2. It is important to point out that, in this research, the proposed non-local degradation model has been employed with a neighborhood parameter, $C_\epsilon psilon$, of 1.5. This is an important difference with the model proposed for the original example, which evaluates the degradation locally in an Arbitrary Eulerian-Lagrangian (ALE) configuration.

In addition, the geometry and boundary conditions can be seen in Fig. 5. About the latest, two boundary conditions have been considered. In the first one, Γ_1 in Fig. 5, both vertical and horizontal displacements are constrained. In Γ_2 a horizontal displacement of 10 meters is imposed gradually from 0 to 1000 s.

The stress behavior is analyzed in Fig. 6. In order to assess the performance of the proposed algorithm, similar to the figure proposed by Zhang *et al.*[47], in Fig. 6 a dimensionless measurement of the shear stress is plotted. It is calculated as a relative increment from the residual shear strength τ_{95} and divided by the maximum increment, measured from the initial (or peak) strength to the residual one, $\tau_p - \tau_{95}$. On the other hand, in the abscissa, the dimensionless distance from the beginning of the degradation is plotted. Thus, the degradation starts from 0 until reaching the τ_{95} at distance 1.

Results obtained in this research and the ones obtained by Zhang *et al.*[47] are not coincident since they are different approaches; however, the overall trend, mainly after the beginning of the degradation, is similar to the reference research. This application allows us to assess the performance of a degraded layer of soft clay, which has been proved to perform similar to other validated studies.
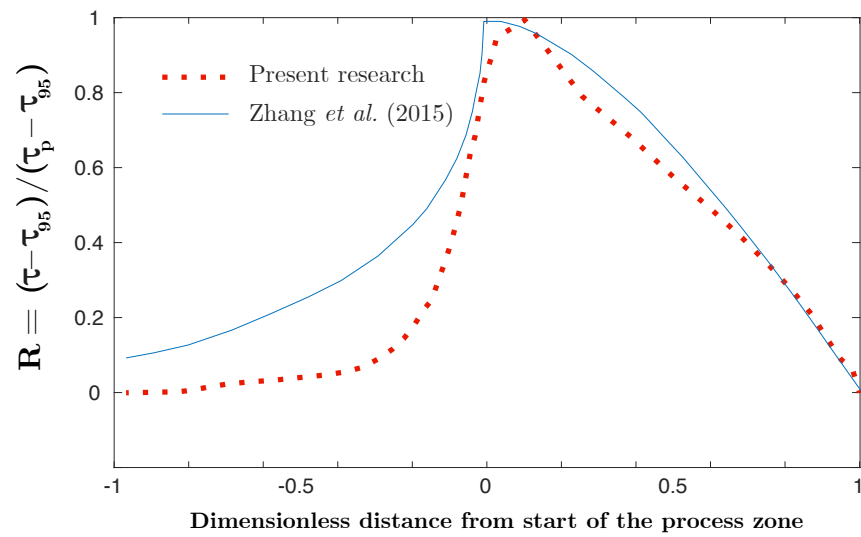
Figure 6. Geometry and loading conditions of the shear degradation problem.
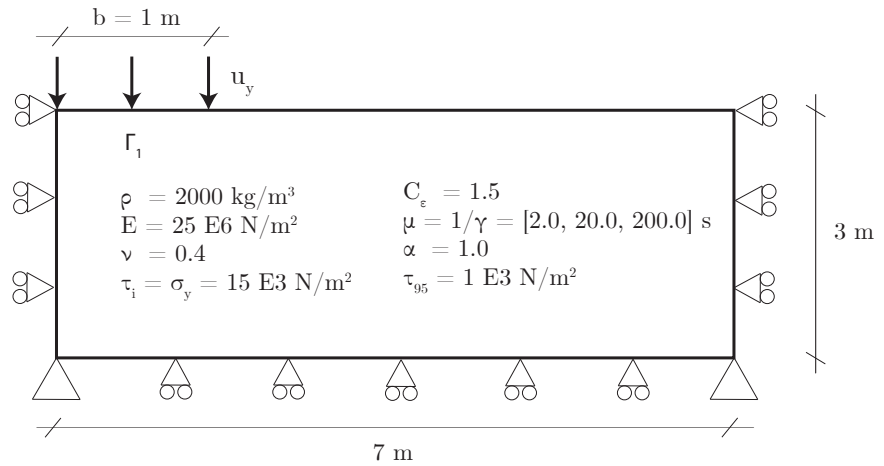
4.2. Strip footing load

Following, the behavior of the soil under different loading rates of a strip footing is analyzed. Similarly, the viscous properties of the soil are varied in order to extend the analysis to the behavior of the soil. This classic problem has been extensively used to verify the solutions provided by numerical models under viscoplastic conditions. The two main features to assess are the mechanism of failure and the behavior of the reaction forces at different viscoplastic scenarios. These results have been previously presented in the work of Pastor and coworkers [35,58], where the loading is applied as an incremental velocity downwards at the base of the strip footing. In the present research, the loading is applied as a negative displacement according to the following expression:

$$u_y = u_f \left(t/t_f \right)^2,$$

where $u_f = 0.04$ m. and $t_f = 4$ s. The geometry and soil parameters can be seen in Fig.7. Parameters of the Eigendegradation algorithm are also depicted. Opposite to the previous application, in this case there is no weak layer, acting the whole domain as a viscoplastic degradable soil.

The first calculation is made by activating the degradation part. This degradation acts as a softening of the material following the proposed exponential expression. It is known how the softening of the material boosts the formation of shear bands. In Fig. 8 the mechanism of failure is depicted. In [58], there is a study of the influence of the discretization size and the parameters of the meshfree model. Optimal options achieved in the aforementioned study have been activated here.

In order to verify the performance of the full model, different viscous parameters have been employed in the calculation of the failure load of the strip footing. Establishing the sensitivity parameter α as 1.0, the viscous parameter has been varied with different values (see Fig. 7). The obtained results have been depicted in Fig.9 for different values of μ. The smaller the value of the μ parameter (*i.e.* large values of γ), the higher the final loading is obtained from the footing loading, as expected from the viscous model. In addition, in dashed line, the reference value obtained by Navas *et al.* [58] is depicted. This line can be considered as the value of a pseudo-static load is applied, without any rigidization due to the viscous behavior. This value is very close to the one obtained with $\mu = 200$ s.

Figure 7. Geometry, material parameters and loading conditions of the strip footing problem.
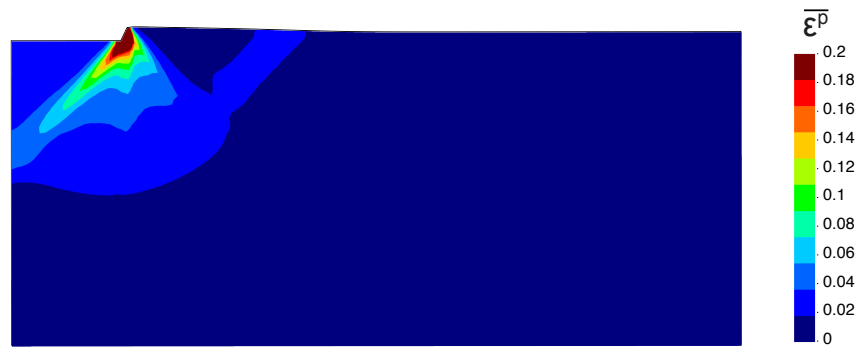

Figure 8. Equivalent plastic deformation of the footing problem using von Mises law with softening through degradation at the final of the simulation.

Similarly, depending on the loading rate, the material can get stiffer and provide bigger response of the reaction forces. Thus, for $\mu = 200$ s., 3 different loading rates have been tested. The obtained results have been depicted in Fig.10 for different values of t_f, being this parameter the final time of application of the imposed displacement $(u_y = u_f \left(t/t_f \right)^2)$. The quicker is the application of the displacement, the higher the final loading is obtained from the footing loading, as expected from the viscous model. In addition, in dashed line, the reference pseudo-static value, obtained by Navas *et al.* [58], is depicted also in this figure, being close to the slowest case.
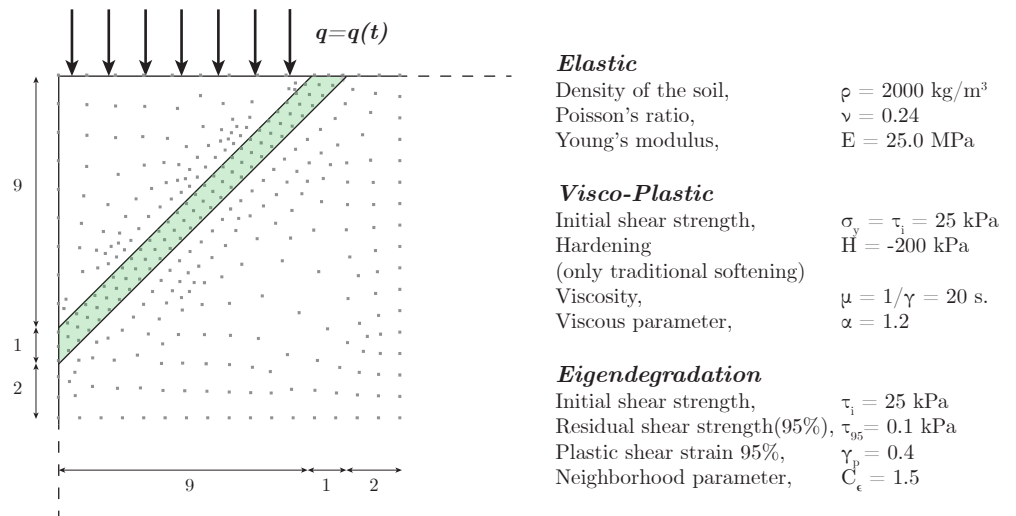
4.3. Vertical cut

This final application allows understanding the potentiality of the proposed methodology. A weak layer is supposed in a soil with a vertical cut on the left side. This weak layer is located forming a 45° angle, as it is sketched in Fig. 11. This layer, whose thick is 1 meter, will be considered plastic. Von Mises yield surface is employed, being its degradation modeled through both *Eigendegradation* and traditional softening, in order to assess the performance of the first one against the latter. Out of the weak layer, the soil is considered elastic since its failure is far from the failure of the weak layer. Parameters of both models are presented in the right part of Fig. 11. In the traditional softening model,
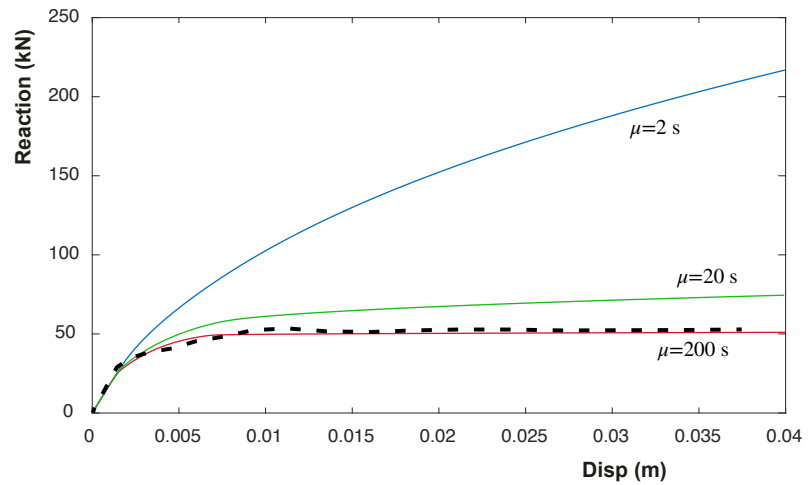
Figure 9. Obtained reaction with different μ values for the problem of the strip footing using viscoplastic von Mises law. The dashed line represents the pseudo-static behavior.
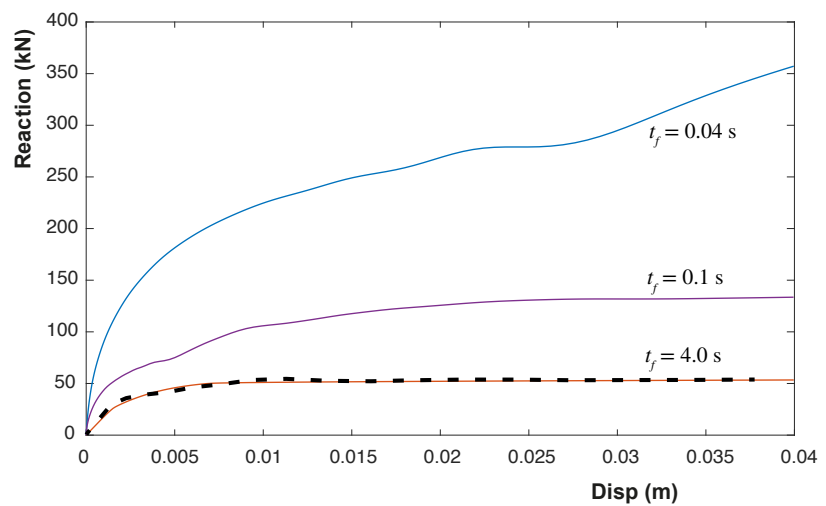
Figure 10. Obtained reaction with different loading rates for the problem of the strip footing using viscoplastic von Mises law, being t_f the final time of the application of the load. The dashed line represents the pseudo-static behavior.

Figure 11. Left:Geometry of the vertical cut analyzed through *Eigendegradation* and softening models and the location of the weak layer and the loaded zone. (Units in meters). Right: parameters of the employed models.

no Eigendegradation parameters are needed. Instead, a negative hardening of 200 kPa is employed. This parameter is not employed in the Eigendegradation simulation.

The soil can be considered infinite on the right and on the bottom of the model; thus, any movement in these directions is prevented. The 12 first meters are modeled for the sake of simplicity.

The top left part is loaded by a surface load, as it is shown in Fig. 11. This load is composed by two different waves, as it is sketched in Fig. 12.

Both waves follow the expression:

$$q_\alpha(t) = A_\alpha \cdot [1 - cos(\omega_\alpha t)]$$

where α varies for each of both loads. The bigger load is the one that provokes the triggering of the plastic mechanism. It can be considered as an abnormal scenario that may lead to catastrophic consequences in the short or in the long time. Their parameters are $A_1 = 11$ kPa and $\omega_1 = 0.1\pi$ rad/s. This load is applied only in the first 20 seconds of simulation. The secondary load is of a lower magnitude. It could be considered as a usual load that the soil suffers permanently and is not capable to provoke the breakage of the slope by itself. The amplitude of this load is half of the first one, $A_2 = 5.5$ kPa and the frequency is much higher, $\omega_2 = 3\pi$ rad/s. This load is maintained through the 80 s. of the simulation.

Following, in Fig. 13, the evolution of both shear strength and the equivalent plastic strain are depicted along the time for both Eigendegradation and softening models. On the left, the shear strength is plotted. The first part of the figure is leaded by the first load: the material reach the yield stress close to 10 s. and start to decrease the strength till 15 s. Both materials, until this point, behave similarly. Observing the right figure, we can see how both models obtain plastic strain until 15 s. as well. Obviously, the amount of shear strain is different since one law is logarithmic (eigendegradation) and the other one is linear. After this point, the eigendegradation model accumulates shear strain (elastic in this case) that makes the shear strength to decrease. This elastic shear strain comes from the second law (the one with small amplitude). We know that is elastic strain since, in the right figure, no accumulated plastic strain is obtained from 15 s. to 50 s. From this point on, the equivalent plastic strain increases drastically. It is translated in an increment of the descent of the yield stress. However, since this accumulated strain provoked by the
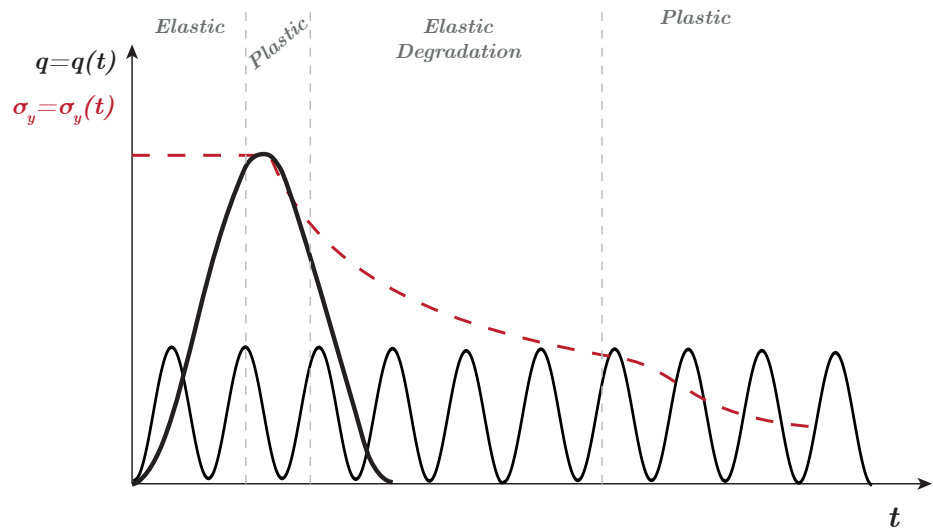
Figure 12. Scheme of the load and the yield strength along the time.

second load is elastic, no variation of the shear strength with the traditional softening model is observed.

Another observation that arises from Fig. 13 is the capability of the model of being sensitive to both loading and unloading conditions of the load, *i.e.*, any variation of the strain, positive or negative, makes the material to degrade and lose shear strength. It is seen in the slope of the yield stress curve from 15 to 50 s., that remains constant along the whole loading cycle, equal in the loading or unloading branch.

Finally, in Fig. 14, the distribution of the equivalent plastic strain in the deformed model at 4 different times is depicted. The chosen moments were: i) the peak of the first load (around 15 s.), ii) the beginning of the secondary plastification of the material (50 s.), iii) moments before the failure of the slope (75 s.) and iv) moments after the triggering of the slope.

5. Conclusions

A visco-plastic degradation model has been proposed in order to simulate the behavior of layers of soft clays. The non-local performance of the proposed algorithm has been carried out following concepts of non-local meshfree models capable to reproduce both brittle (Eigenerosion) and quasi-brittle (Eigensoftening) behaviors. Thus, the proposed algorithm takes the name of *Eigendegradation*.

Two main properties defined the proposed constitutive model: softening due to degradation and visco-plastic behavior. Thus, two different examples are provided in order to validate both properties.

The first example reproduces a shear test of a soil with a thin soft layer. This test shows the performance of the degradation behavior from the beginning of the reduction of the shear strength to the final of this reduction, obtaining a residual strength. This result has been compared to other similar work of degradation of clays, obtaining very close curves, what let us think the behavior of the proposed algorithm when modeling this material is correct.

The second example studies the behavior of a soil loaded by a strip footing. In this case, the viscoplastic concept is the one to be assessed. Since the von Mises yield surface is employed, the traditional Prandtl mechanism is obtained. Moreover, a hardening behavior is observed either when the viscosity becomes higher or when the load is applied quicker. This example allows us to validate the viscous behavior, as well as to
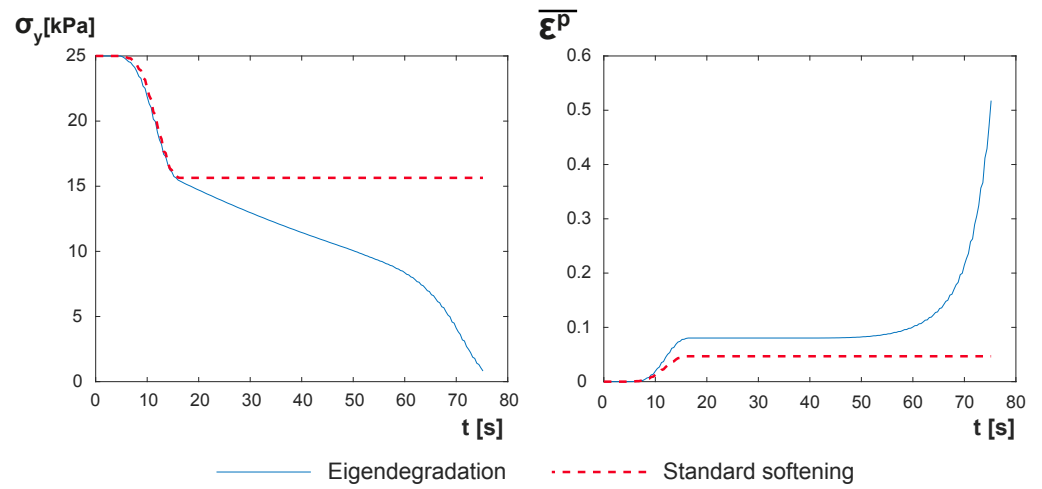
Figure 13. Evolution of the shear strength and the equivalent plastic strain along the time for both Eigendegradation and softening models.
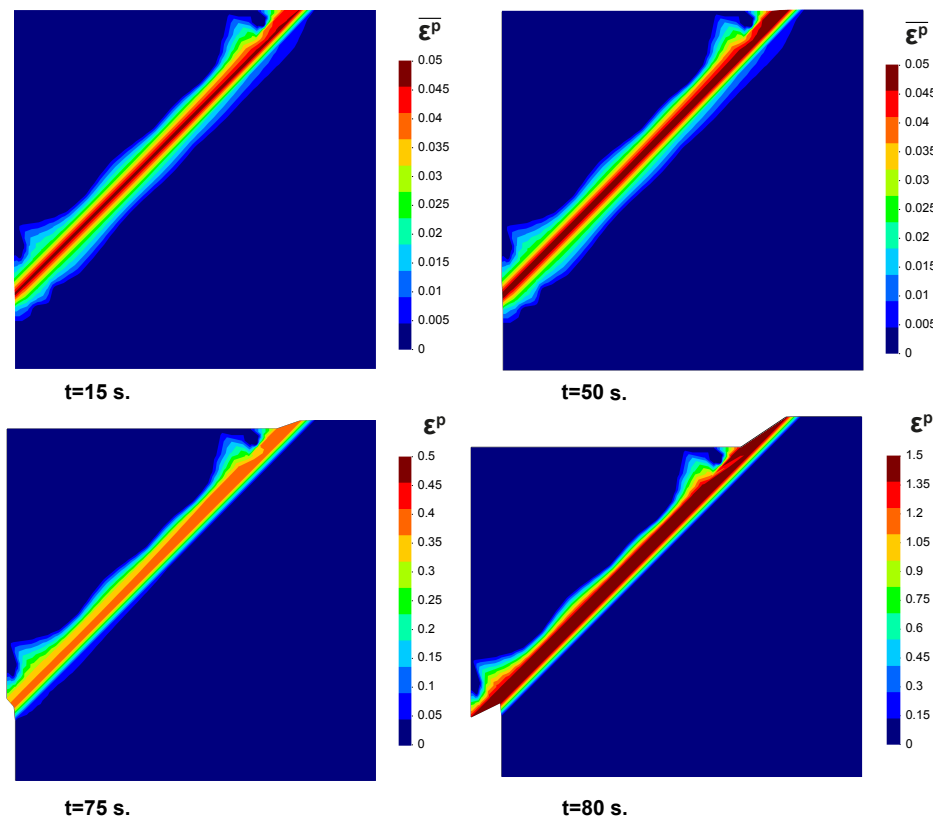
Figure 14. Distribution of the equivalent plastic strain in the deformed model at 4 different times.

verify that the degradation acts as a softening of the material that helps to define clearer the shear bands formed in the plastic mechanism.

Finally, a vertical cut of soil is modeled. This soil contains a 45° soft layer. A compound load is applied, being the first part what makes the beginning of the degradation of the material and the last part the one that makes the whole degradation of the shear strength and the final failure of the slope. In comparison with a traditional softening law, the proposed one is capable to produce degradation with elastic accumulated strain, being able the accumulation by both loading or unloading conditions. This behavior is seen in many failures of these kinds of soft layers, where a load much lower than the critical one but held in the time produces the fatigue of the material and the final failure of the soil structure.

The present algorithm has performed successfully with the proposed applications. Further research can be made in order to be able to reproduce a wide range of problems. First of all, this model should be calibrated against experimental tests such as the shear test. Moreover, only the von Mises yield surface has been validated in this manuscript. Although it is able to reproduce the undrained conditions of the soil, more sophisticated yield surfaces, such as the Cam-Clay one, would improve the type of problems to be modeled. The soil should also be modeled as a biphase material, including the water in the formulation of the problem. Finally, some other spatial discretization, such as FEM or MPM, could be employed to assess the performance of this algorithm.

Author Contributions: Conceptualization, S. López-Querol. and D. Manzanal; software and validation, P.Navas; resources, A. Yagüe; supervision, M.Martín-Stickle. All authors have read and agreed to the published version of the manuscript.

Conflicts of Interest: The authors declare no conflict of interest.

Abbreviations

The following abbreviations are used in this manuscript:

FEM	Finite Element Method
OTM	Optimal Transportation Meshfree
SPH	Smooth Particle Hydrodynamics
MPM	Material Point Method
ALE	Arbitrary Eulerian-Lagrangian

References

1. Drucker, D.C.; Prager, W. Soil mechanics and plastic analysis for limit design. *Quarterly of Applied Mathematics* **1952**, *10(2)*, 157–165.
2. Darve, F.; Laouafa, F. Instabilities in granular materials and application to landslides. *Mechanics of Cohesive-frictional Materials* **2000**, *5*, 627–652,
3. Pastor, M.; Manzanal, D.; Merodo, J.A.F.; Mira, P.; Blanc, T.; Drempetic, V.; Pastor, M.J.; Haddad, B.; Sánchez, M. From solids to fluidized soils: diffuse failure mechanisms in geostructures with applications to fast catastrophic landslides. *Granular Matter* **2009**, *12*, 211–228. doi:10.1007/s10035-009-0152-4.
4. Ledesma, O.; Manzanal, D.; Sfriso, A. Formulation and numerical implementation of a state parameter-based generalized plasticity model for mine tailings. *Computers and Geotechnics* **2021**, *135*, 104158. doi:10.1016/j.compgeo.2021.104158.
5. Ledesma, O.; Sfriso, A.; Manzanal, D. Procedure for assessing the liquefaction vulnerability of tailings dams. *Computers and Geotechnics* **2022**, *144*, 104632. doi: 10.1016/j.compgeo.2022.104632.

6. Laouafa, F.; Darve, F. Modelling of slope failure by a material instability mechanism. *Computers and Geotechnics* **2002**, *29*, 301–325. doi:10.1016/s0266-352x(01)00030-1.

7. Fernández Merodo, J.A.; Pastor, M.; Mira, P.; Tonni, L.; Herreros, M.I.; Gonzalez, E.; Tamagnini, R.; Merodo, J.A.F.; Pastor, M.; Mira, P.; Tonni, L.; Herreros, M.I.; Gonzalez, E.; Tamagnini, R. Modelling of diffuse failure mechanisms of catastrophic landslides. *Computer Methods in Applied Mechanics and Engineering* **2004**, *193*, 2911–2939.

8. López-Querol, S.; Blázquez, R. Liquefaction and cyclic mobility model in saturated granular media. *International Journal for Numerical and Analytical Methods in Geomechanics* **2006**, *30*, 413–439. doi:10.1002/nag.488.

9. Manzanal, D.; Bertelli, S.; Lopez-Querol, S.; Rossetto, T.; Mira, P. Influence of fines content on liquefaction from a critical state framework: the Christchurch earthquake case study. *Bulletin of Engineering Geology and the Environment* **2021**, *80*, 4871–4889. doi:10.1007/s10064-021-02217-2.

10. Manzanal, D.; Drempetic, V.; Haddad, B.; Pastor, M.; Stickle, M.M.; Mira, P. Application of a New Rheological Model to Rock Avalanches: An SPH Approach. *Rock Mechanics and Rock Engineering* **2016**, *49*, 2353–2372. doi:10.1007/s00603-015-0909-5.

11. Dutto, P.; Stickle, M.; Pastor, M.; Manzanal, D.; Yague, A.; Tayyebi, S.M.; Lin, C.; Elizalde, M. Modelling of Fluidised Geomaterials: The Case of the Aberfan and the Gypsum Tailings Impoundment Flowslides. *Materials* **2017**, *10*, 562. doi:10.3390/ma10050562.

12. Longo, A.; Pastor, M.; Sanavia, L.; Manzanal, D.; Stickle, M.M.; Lin, C.; Yague, A.; Tayyebi, S.M. A depth average SPH model includingbiμ/i/b(iI/i) rheology and crushing for rock avalanches. *International Journal for Numerical and Analytical Methods in Geomechanics* **2019**, *43*, 833–857. doi:10.1002/nag.2912.

13. Lin, C.; Pastor, M.; Yague, A.; Tayyebi, S.M.; Stickle, M.M.; Manzanal, D.; Li, T.; Liu, X. A depth-integrated SPH model for debris floods: application to Lo Wai (Hong Kong) debris flood of August 2005. *Géotechnique* **2019**, *69*, 1035–1055. doi:10.1680/jgeot.17.p.267.

14. Pastor, M.; Yague, A.; Stickle, M.; Manzanal, D.; Mira, P. A two-phase SPH model for debris flow propagation. *International Journal for Numerical and Analytical Methods in Geomechanics* **2017**, *42*, 418–448. doi:10.1002/nag.2748.

15. Pastor, M.; Tayyebi, S.M.; Stickle, M.M.; Yag´ue, A.; Molinos, M.; Navas, P.; Manzanal, D. A depth integrated, coupled, two-phase model for debris flow propagation. *Acta Geotechnica* **2021**, *Online*. doi:10.1007/s11440-020-01114-4.

16. Zabala, F.; Alonso, E.E. Progressive failure of Aznalcóllar dam using the material point method. *Géotechnique* **2011**, pp. 795–808. doi:10.1680/geot.9.P.134.

17. Yerro, A.; Alonso, E.E.; Pinyol, N.M. The material point method for unsaturated soils. *Geotechnique* **2015**, *65*, 201–217. doi:10.1680/geot.14.P.163.

18. Yerro, A.; Alonso, E.E.; Pinyol, N.M. Run-out of landslides in brittle soils. *Computers and Geotechnics* **2016**, *80*, 427–439.

19. Feng, K.; Wang, G.; Huang, D.; Jin, F. Material point method for large-deformation modeling of coseismic landslide and liquefaction-induced dam failure. *Soil Dynamics and Earthquake Engineering* **2021**, *150*, 106907. doi:https://doi.org/10.1016/j.soildyn.2021.106907.

20. Sizkow, S.F.; El Shamy, U. SPH-DEM simulations of saturated granular soils liquefaction incorporating particles of irregular shape. *Computers and Geotechnics* **2021**, *134*, 104060. doi:https://doi.org/10.1016/j.compgeo.2021.104060.

21. Rice, J.R. The Initiation and growth of shear band. In Plasticity and soil mechanics (ed. A. C. Palmer). Cambridge: Cambridge University Engineering Department., 1973, pp. 263–274.

22. Desrues, J. La localisation de la déformation dans les milieux granulaires,. PhD thesis, 1984.

23. Sulem, J.; Vardoulakis, I. *Bifurcation Analysis in Geomechanics*; CRC Press, 1995. doi:10.1201/9781482269383.

24. Wang, W.; Sluys, L.; De Borst, R. Viscoplasticity for instabilities due to strain softening and strain-rate softening. *International Journal for Numerical Methods in Engineering* **1997**, *40*, 3839–3864.

25. Gutiérrez, M.A.; De Borst, R. Numerical analysis of localization using a viscoplastic regularization: influence of stochastic material defects. *International Journal for Numerical Methods in Engineering* **1999**, *44*, 1823–1841,

26. Bjerrum, L. Engineering Geology of Norwegian Normally-Consolidated Marine Clays as Related to Settlements of Buildings. *Géotechnique* **1967**, *17*, 83–118. doi:10.1680/geot.1967.17.2.83.

27. Kim, Y.T.; Leroueil, S. Modeling the viscoplastic behaviour of clays during consolidation: application to Berthierville clay in both laboratory and field conditions. *Canadian Geotechnical Journal* **2001**, *38*, 484–497.

28. In *Creep of Soils and Related Phenomena*; Developments in Geotechnical Engineering, Elsevier, 1992; pp. 3–422.

29. Manzanal, D.; Pastor, M.; Javanmardi, Y.; Fernández Merodo, J.A.; Mira, P.; Martín Stickle, M.; Yagüe, A. *A reference state curve to define the state of soils over a wide range of pressures and densities*, coupled an ed.; 2015.

30. Adachi, T.; Okano, M. A Constitutive Equation for Normally Consolidated Clay. *Soils and Foundations* **1974**, *14*, 69–73. doi:https://doi.org/10.3208/sandf1972.14.4_55.

31. Heeres, O.M.; Suiker, A.S.; de Borst, R. A comparison between the Perzyna viscoplastic model and the Consistency viscoplastic model. *European Journal of Mechanics - A/Solids* **2002**, *21*, 1–12. doi:https://doi.org/10.1016/S0997-7538(01)01188-3.

32. Perzyna, P. Fundamental Problems in Viscoplasticity. *Advances in Applied Mechanics* **1966**, *9*, 243–377.

33. Naghdi, P.M.; Murch, S.A. On the Mechanical Behavior of Viscoelastic/Plastic Solids. *Journal of Applied Mechanics* **1963**, *30*, 321–328. doi:10.1115/1.3636556.

34. Nova. A viscoplastic constitutive model for normally consolidated clays. *International union of theoretical and applied mechanics conference on deformation and failure of granular materials.Delft, Netherlands.* **1982**, pp. 287–295.

35. Blanc, T.; Pastor, M. A stablized {Runge-Kutta, Taylor} smoothed particle hydrodynamics algorithm for large deformation problems in dynamics. *International Journal for Numerical Methods in Engineering* **2012**, *91*, 1427–1458. doi:10.1002/nme.

36. Navas, P.; Yu, R.C.; Li, B.; Ruiz, G. Modeling the dynamic fracture in concrete: an eigensoftening meshfree approach. *International Journal of Impact Engineering* **2018**, *113*, 9–20. doi:10.1016/j.ijimpeng.2017.11.004.

37. Molinos, M.; Navas, P.; Manzanal, D.; Pastor, M. Local Maximum Entropy Material Point Method applied to quasi-brittle fracture. *Engineering Fracture Mechanics* **2021**, *241*, 107394. doi:10.1016/j.engfracmech.2020.107394.

38. de Souza Neto, E.A.; Pires, F.M.; Owen, D.R.J.; Andrade Pires, F.M. F-bar-based linear triangles and tetrahedra for finte strain analysis of nearly incompressible solids. {Part I:} formulation and benchmarking. *International Journal for Numerical Methods in Engineering* **2005**, *62*, 353–383. doi:10.1002/nme.1187.

39. Owen, D.R.J.; Hinton, E. *Finite elements in plasticity—theory and practice*; Pineridge Press, Swansea, 1981; p. 603. doi:10.1002/nme.1620170712.

40. Schmidt, B.; Fraternali, F.; Ortiz, M. Eigenfracture: an eigendeformation approach to variational fracture. *SIAM J. Multiscale Model. Simul.* **2009**, *7*, 1237–1266. doi:10.1137/080712568.

41. Pandolfi, A.; Ortiz, M. An eigenerosion approach to brittle fracture. *International Journal for Numerical Methods in Engineering* **2012**, *92*, 694–714. doi:10.1002/nme.

42. Li, B.; Kadane, A.; Ravichandran, G.; Ortiz, M.; Kidane, A. Verification and validation of the optimal-transportation meshfree (OTM) simulation of terminal ballistics. *International Journal of Impact Engineering* **2012**, *42*, 25–36. doi:10.1016/j.ijimpeng.2011.11.003.

43. Pandolfi, A.; Li, B.; Ortiz, M. Modeling fracture by material-point erosion. *International Journal of fracture* **2013**, *184*, 3–16. doi:10.1007/s10704-012-9788-x.

44. Yu, R.C.; Navas, P.; Ruiz, G. Meshfree modeling of the dynamic mixed-mode fracture in FRC through an eigensoftening approach. *Engineering Structures* **2018**, *172*, 94–104. doi:10.1016/j.engstruct.2018.06.010.

45. Bažant, Z.P.; Oh, B.H. Crack band theory for fracture in concrete. *Materials and Structures* **1983**, *16*, 155–177.

46. Bažant, Z.P.; Planas, J. *Fracture and Size Effect in Concrete and Other Quasibrittle Materials*; New directions in Civil Engineering, CRC Press, Boca Raton, Florida, USA, 2019; pp. 1–170. doi:10.1201/9780203756799.

47. Zhang, W.; Wang, D.; Randolph, M.; Puzrin, A., M. Catastrophic failure in planar landslides with a fully softened weak zone. *Géotechnique* **2015**, *65*, 755–769. doi:10.1680/geot14.P.218.

48. Wang, L.; Zhang, X.; Tinti, S. Large deformation dynamic analysis of progressive failure in layered clayey slopes under seismic loading using the particle finite element method. *Acta Geotechnica* **2021**, *16*, 2435–2448. doi:10.1007/s11440-021-01142-8.

49. Singh, V.; Stanier, S.; Bienen, B.; Randolph, M.F. Modelling the behaviour of sensitive clays experiencing large deformations using non-local regularisation techniques. *Computers and Geotechnics* **2021**, *133*, 104025. doi:10.1016/j.compgeo.2021.104025.

50. Li, B.; Habbal, F.; Ortiz, M. Optimal transportation meshfree approximation schemes for fluid and plastic flows. *International Journal for Numerical Methods in Engineering* **2010**, *83*, 1541–1579. doi:10.1002/nme.

51. Li, B.; Stalzer, M.; Ortiz, M. A massively parallel implementation of the Optimal Transportation Meshfree (pOTM) method for explicit solid dynamics. *International Journal for Numerical Methods in Engineering* **2014**, *100*, 40–61.

52. Huang, D.; Weißenfels, C.; Wriggers, P. Modelling of serrated chip formation processes using the stabilized optimal transportation meshfree method. *International Journal of Mechanical Sciences* **2019**, *155*, 323–333. doi:10.1016/j.ijmecsci.2019.03.005.

53. Navas, P.; Manzanal, D.; Martín Stickle, M.; Pastor, M.; Molinos, M. Meshfree modeling of cyclic behavior of sands within large strain Generalized Plasticity Framework. *Computers and Geotechnics* **2020**, *122*, 103538. doi:10.1016/j.compgeo.2020.103538.

54. Navas, P.; Pastor, M.; Yagüe, A.; Stickle, M.M.; Manzanal, D.; Molinos, M. Fluid stabilization of the u-w Biot's formulation at large strain. *International Journal for Numerical and Analytical Methods in Geomechanics* **2021**, *45*, 336–352. doi:https://doi.org/10.1002/nag.3158.

55. Arroyo, M.; Ortiz, M. Local maximum-entropy approximation schemes: a seamless bridge between finite elements and meshfree methods. *International Journal for Numerical Methods in Engineering* **2006**, *65*, 2167–2202. doi:10.1002/nme.1534.

56. Kontoe, S. Developement of time integration schemes and advanced boundary conditions for dynamic geotechnical analysis. PhD thesis, D. thesis, 2006.

57. Wriggers, P. *Nonlinear Finite Element Methods*; Vol. 2008, Springer, 2008.

58. Navas, P.; López-Querol, S.; Yu, R.C.; Pastor, M. Optimal transportation meshfree method in geotechnical engineering problems under large deformation regime. *International Journal for Numerical Methods in Engineering* **2018**, *115*, 1217–1240. doi:10.1002/nme.5841.